DRIVETRAIN INFLUENCE ON THE LEAD-LAG MODES OF HINGELESS HELICOPTER ROTORS

Felix Weiss, Christoph Kessler

Felix.Weiss@dlr.de, German Aerospace Center (DLR), Germany

Abstract

Structural couplings between the flexible main rotor and the flexible drivetrain of the Bo105 helicopter are investigated by numerical simulation. For this purpose, the rotor hub constraint $\Omega = const.$ is dropped and a drivetrain model, consisting of discrete inertia elements and intermediate flexible elements, is connected to the hub. By use of the multibody-software SIMPACK, the coupled rotor-drivetrain system is linearized and the Eigenmodes are compared to those obtained with a constrained rotor hub. The drivetrain has a significant influence on the shapes and Eigenfrequencies of the collective lead-lag modes. While the first collective lead-lag Eigenfrequency is raised by the finite drivetrain inertia, the second is lowered due to drivetrain flexibility. To assess the influence of modeling inaccuracies on the observed couplings, the study is complemented by a sensitivity analysis. Rotor blade mass axis offset, blade pitch (causing elastic coupling) and blade precone angle have only weak influence on the coupled modes. In contrast, variations of drivetrain inertia and stiffness strongly affect the Eigenfrequencies of the coupled rotor-drivetrain modes.

NOTATION

General symbols

Li		i-th blade lead-lag mode
Fi		i-th blade flap mode
Ti		i-th blade torsion mode
$\mathrm{RD_X}$		rotor-drivetrain mode X
Ω	(rad/s)	rotor hub rotational speed
Ω_{ref}	(rad/s)	nominal rotational rotor speed
ω	(rad/s)	Eigenfrequency

Symbols of main rotor model

$J^{\mathrm{elem}}_{\mathrm{flap}}$	(kgm^2)	flapwise blade element inertia
$J^{\mathrm{elem}}_{\mathrm{lag}}$	(kgm^2)	lagwise blade element inertia
$M^{\mathrm{elem}}_{\mathrm{P}}$	(Nm)	blade el. propeller moment
θ^{elem}	(rad)	blade element pitch angle

Symbols of drivetrain model

b_r	(m)	tooth width of wheel r
c_r	(N/m)	translatory gear stiffness of wheel r
c_γ	(N/m^2)	specific gear mesh stiffness
$d_{0,r}$	(m)	pitch diameter of wheel r
G	(N/m^2)	shear modulus
$I_{\mathrm{T},p}$	(m^4)	torsion constant of shaft segment p
J	(kgm^2)	inertia (of inertia element)
J_{DT}	(kgm^2)	condensed drivetrain inertia
J_p	(kgm^2)	inertia of shaft segment p
k	(Nm/rad)	stiffness (of flexible element)
k_{DT}	(Nm/rad)	condensed drivetr. stiffness
k_p	(Nm/rad)	stiffness of shaft segment p
k_r^{stage}	(Nm/rad)	rotational stiffness of gear stage with respect to rotation of wheel r
ℓ_p	(m)	length of shaft segment p
m_p	(kg)	mass of shaft segment p
n_{planets}		number of planet wheels
R_p	(m)	outer radius of shaft seg. p
r_p	(m)	inner radius of shaft seg. p
β_r	(rad)	helix angle of wheel r
Ω_J	(rad/s)	rotational speed of inertia element J
Ω_k	(rad/s)	rotational speed of stiffness element k
$()^{\mathrm{accu}}$		accumulated
$()^{\mathrm{ad}}$		adapted (by iteration)
$()_{\mathrm{red}}$		reduced

1. INTRODUCTION

Since the early developments of rotary wing aircraft in the late 19th century, helicopters have made tremendous progress in performance, handling qualities, comfort, reliability, and efficiency. Some additional features make helicopters especially useful for many missions, which to date cannot be performed by any other contemporary series production aircraft. These include their capabilities to hover, to climb or descend vertically or almost vertically, to fly slowly in any horizontal direction (even backwards), and to still maintain good performances, handling qualities and manoeuvrability. These advantages, but also their relatively small outer dimensions, allow helicopters to fly at low altitudes between obstacles and to land almost everywhere, even in confined areas. This is why helicopters have conquered their niche in the aircraft market.

Despite the undoubtedly increased maturity of helicopters, some challenges still remain. These are for instance high noise levels, high vibration levels, high demands on hover figure of merit and high speed forward flight, and hence limited capabilities in terms of maximum speed and range. Another challenge especially for the designer remains to precicely determine component loads for their design. This also and particularly applies to the rotor.

The proper determination of rotor blade loads is an essential capability in the development of helicopters. Wind tunnel experiments and numerical simulations enable blade load predictions prior to the first flight of the entirely designed and built helicopter, and thus, contribute to a time- and cost-efficient development process.

The loads correlation between predictions and flight test measurements is generally good in blade flap direction, but poor in lead-lag direction, as shown for wind tunnel experiments[1] and for simulations[2]. Potential reasons for this discrepancy, such as the aerodynamic model[3], the structural blade model[4], actuation system modeling[5] or lag damper modeling[2] have been investigated. Though, the source of errors has not been found yet.

Largely unexplored is the influence of the drivetrain, which consists of mast, main gearbox, engines, tail rotor shaft and tail rotor. Due to couplings in the rotor hub's rotational degree of freedom, torsional drivetrain dynamics is likely to affect the lead-lag loads of the blades. Recently, this issue was taken up in several simulation studies with respect to the fully articulated rotor system of the UH60-A helicopter. A freely rotating, modally reduced torsional drivetrain system was coupled to the main rotor[6], showing notable differences in lead-lag loads compared to a baseline case with constrained rotor hub. In two further studies, drivetrain models were included in rotor simulation to improve correlation with flight test data[7,8]. In both cases, the large discrepancies in the lead-lag loads could not be traced to drivetrain influence. Though, both drivetrain models featured constrained engines, which is an invalid boundary condition and restricts the validity of results.

Moreover, none of the mentioned studies presented the particular physical effects behind rotor-drivetrain coupling. Besides, drivetrain influence on hingeless rotor systems has not been adressed yet. Due to direct moment transmission at the blade attachment, hingeless rotors are expected to be more influenced by the drivetrain than articulated rotors are.

As a first step to thoroughly understand drivetrain influence on lead-lag dynamics of hingeless rotors, the complete rotor-drivetrain structure of the Bo105 helicopter is modeled and analyzed in the present study.

2. DRIVETRAIN MODEL

The drivetrain model consists of discrete inertia elements J and connecting flexible elements k representing torsional flexibility of shafts and the flexibility of gear meshes. Related parameters of the mast and main gearbox are determined based on technical specifications provided by the gearbox manufacturer as described in chapters 2.1 and 2.2. Tail rotor inertia and shaft stiffness have been supplied by Airbus Helicopters Germany. The inertia of the engines' low pressure stages connected to the main gearbox drive shafts has been measured at DLR.

2.1. Gearbox Inertias and Shaft Stiffnesses

Parameter identification of gearbox inertias and stiffnesses is based on the methods described by Laschet[9] and Dresig[10], where multiply stepped solid shafts are split into discrete inertias and torsional stiffnesses. However, shafts of helicopter drivetrains are usually hollow and feature integrated gear teeth and bearing seats. Thus, the shafts are approximated through hollow, cylindrical segments. This is illustrated in Figure 1 by the example of the intermediate shaft, which is split into seven segments.

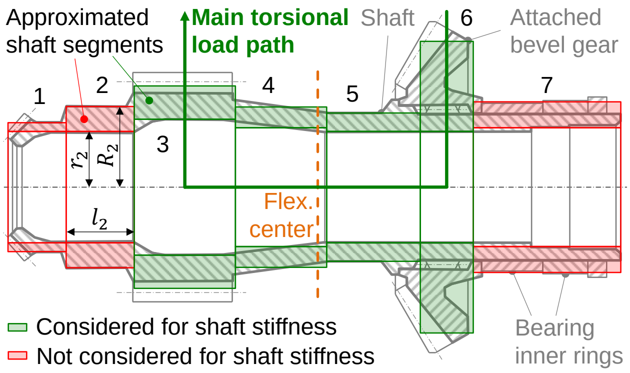

Figure 1: Inertia and stiffness calculation of the intermediate shaft on the basis of approximated shaft segments

Despite the segmentation of the shaft, it shall be modeled by only one stiffness element and two surrounding inertia elements to keep the overall drivetrain model simple. For determination of the shaft torsional stiffness, only the segments in the main torsional load path* (green) between the gears are serially connected. The segment stiffnesses

$$(1)\quad k_p = \frac{G \cdot I_{\mathrm{T},p}}{\ell_p} \qquad p = 1, 2, \ldots, 7 \text{ in Figure 1}$$

are computed from shear modulus G, sectional torsion constant $I_{\mathrm{T},p}$ and segment length ℓ_p. The stiffness of the entire shaft k is obtained from

$$(2)\quad \frac{1}{k} = \sum_{p=p_{\min}}^{p_{\max}} \frac{1}{k_p}. \qquad \left.\begin{array}{l} p_{\min} = 3 \\ p_{\max} = 6 \end{array}\right\} \text{ in Figure 1}$$

Unlike for calculation of stiffness, all segments contribute to the inertia of the shaft. Segment inertias J_p are calculated from segment mass m_p as well as outer and inner radii R_p and r_p.

$$(3)\quad J_p = \frac{1}{2} \cdot m_p \cdot \left(R_p^2 + r_p^2\right) \qquad p = 1, 2, \ldots, 7 \text{ in Fig. 1}$$

Since the shaft is represented by two inertias J, the individual segment inertias J_p need to be placed on either side of the flexible element. This allocation is defined by the axial center of flexibility† (orange line). In the example of Figure 1, segment inertias J_1, J_2 and J_3 are assigned to the output side of the shaft (left), while J_5, J_6 and J_7 are related to the input side (right). J_4 is divided proportionally according to the center of flexibility. By the presented approach, each shaft is eventually defined by one stiffness element k and two surrounding inertia elements J.

*In the example of Figure 1, the additional bevel gear to the left (accessory drive) as well as segments 1, 2 and 7 do not contribute to the flexibility between main rotor and engines, i. e. they do not lie in the main torsional load path.

†The axial center of flexibility is obtained from the mean value of the segment indices in the main torsional load path, weighted by the reciprocal segment stiffnesses.

2.2. Gear Mesh Stiffnesses

Beside shaft flexibilities, the drivetrain model features connections representing the flexible gear meshes. Since the lowest meshing frequency (83 Ω) is above the range of interest for the investigated rotor-drivetrain-couplings, mesh stiffnesses are assumed to be constant.

The determination method follows DIN 3990. According to Laschet[9], the specific gear mesh stiffness lies in the range $c_\gamma = 10 \ldots 20 \cdot 10^9\,\mathrm{N/m^2}$. In view of the lightweight design of helicopter drivetrain gear wheels, the lower bound $c_\gamma = 10 \cdot 10^9\,\mathrm{N/m^2}$ is chosen for all gear mesh stiffnesses. With the tooth width b_r and the helix angle β_r, the translatory stiffness of one gear wheel (subscript r cf. Table 1) at the mesh point is

$$(4)\quad c_r = \frac{c_\gamma \cdot b_r}{\cos \beta_r}.$$

Table 1: Subscript r indicating the gear wheel

Spur and bevel gear stage	$r = \mathrm{in}, \mathrm{out}$
Planetary gear stage	$r = \mathrm{sun}, \mathrm{planet}, \mathrm{ring}$

A gear mesh stiffness element k of the drivetrain model represents the complete gear stage. The rotation reference is given by the input wheel of the stage, indicated by subscript $r = \mathrm{in}$.

$$(5)\quad k = k_{\mathrm{in}}^{\mathrm{stage}} = \frac{\left(\frac{d_{0,\mathrm{in}}}{2}\right)^2}{\frac{1}{c_{\mathrm{in}}} \cdot \frac{1}{c_{\mathrm{out}}}}$$

d_0^{in} is the pitch diameter of the input gear wheel. In the case of a planetary stage, the number of planet wheels n_{planets} has to be considered. The rotation reference is given by the sun wheel, $r = \mathrm{sun}$.

$$(6)\quad k = k_{\mathrm{sun}}^{\mathrm{stage}} = \frac{\left(\frac{d_{0,\mathrm{sun}}}{2}\right)^2 \cdot n_{\mathrm{planets}}}{\frac{1}{c_{\mathrm{sun}}} \cdot \frac{1}{c_{\mathrm{planet}}} \cdot \frac{1}{c_{\mathrm{ring}}}}$$

2.3. The Bo105 Drivetrain

The drivetrain connects the main rotor, the tail rotor, the two engines and the accessories. Figure 2 shows the abstracted drivetrain, modeled by the methods described previously. The 16 inertia elements J are depicted by black horizontal bars. The flexible shafts and gearings k are represented by blue and red links, respectively. The rotor mast (1) is connected to the planet carrier of the planetary stage (2). The sun gear sits on top of the main gearbox core (3). At the bottom of the core (4), the collector stage (5) branches to the left and right intermediate shafts (6). A further bevel gear stage (7) connects the intermediate shafts to the drive shafts (8). The drive shafts are directly coupled to the low pressure stages of the engines. Via the tail rotor drive stage (9) and the connection shaft (10), the long and flexible tailrotor shaft (11) is driven. It includes the intermediate gearbox (IGB) and the tailrotor gearbox (TGB) and ends at the tail rotor.

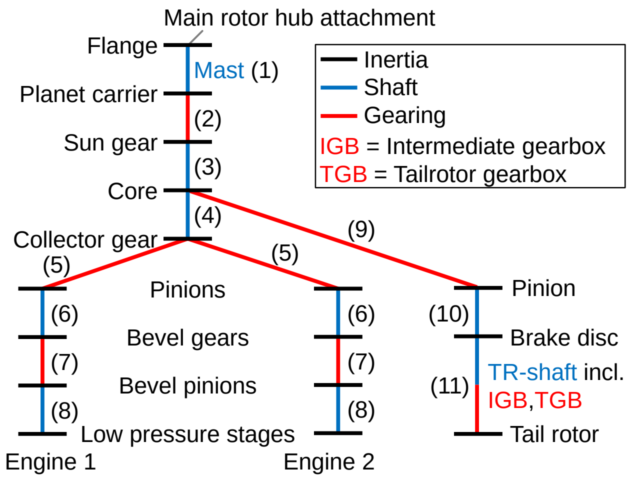

Figure 2: Bo105 drivetrain model

Figure 3 compares the stiffnesses of the flexible drivetrain elements on a logarithmic scale. To account for transmission ratios, all values are reduced to main rotor speed‡. Although the mast (element 1) and the tail rotor shaft (element 11) are by far the most flexible drivetrain components, the neglection of all other flexible parts would lead to an error of 16 % in the overall stiffness between rotor hub and engines. For this reason, flexibility of all shafts and gear meshes is considered.

The largest inertias, summarized in Table 2, are located at the ends of the drivetrain. For comparison, all values are reduced to main rotor speed§. Note that for rotor-drivetrain oscillations, the rotor must not be regarded as a rigid disk. For this reason, the blade inertia is given about the equivalent lead-lag hinge of a rigid surrogate blade model. The value

‡Reduced stiffness[11]: $k_{\text{red}} = (\Omega_k/\Omega)^2 \cdot k$

§Reduced inertia[11]: $J_{\text{red}} = (\Omega_J/\Omega)^2 \cdot J$

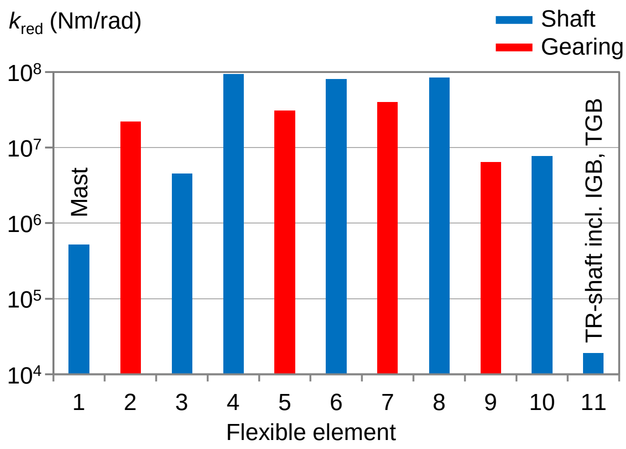

Figure 3: Stiffnesses of flexible elements in the Bo105 drivetrain, reduced to main rotor speed. Element numbers refer to Figure 2

only serves as a rough benchmark, since the node of a coupled rotor-drivetrain mode shape does not coincide with this ficticious lead-lag hinge position in general. As expected, the summed inertia of the four rotor blades is significantly larger than that of any other component. Due to fast rotation, the low pressure stages of the engines feature the second largest reduced inertia (both together about 32 % of the blades' inertia). The ratio of reduced inertias between tail rotor and main rotor blades is about 5 %. All main gearbox components, including the accessories, have an accumulated reduced inertia of less than 3 % of the blades' inertia.

Table 2: Inertias of the Bo105 main rotor and drivetrain, reduced to main rotor speed

	Component	J_{red} (kgm^2)
Rotor	Blades *(about equivalent lead-lag hinges)*	$4 \cdot 128.9 = 515.6$
	Hub & blade roots *(up to equivalent lead-lag hinges)*	8.7
Drivetrain	Engine low pressure stages	$2 \cdot 82.1 = 164.2$
	Tail rotor	25.7
	Main gearbox (summed up)	15.1

3. MAIN ROTOR MODEL

The present study is a pure structural analysis, i. e. no airloads are included. By use of the SIMPACK-internal FE-module SIMBEAM, the rotor blade is modeled as a 1D-Euler-Bernoulli beam, featuring bending deformation in flap and lead-lag direction as well as elastic torsion. Offsets between the mass axis and the elastic axis are taken into account.

Since any deformation in SIMBEAM is linear, the blade is segmented in order to accurately capture higher order effects[12]. A number of 12 blade segments has proved to reliably account for Coriolis-coupling between blade flap and lag motion. Each beam segment is described by one SIMBEAM-body. Element-wise blade discretization and sectional properties are adopted from a validated input file for the finite-element-method (FEM) preprocessor of the in-house tool S4 featuring 52 elements per blade. The distribution of segments and elements is illustrated in Figure 4. The fine elemental discretization in the second segment from the left originates from blade attachment modeling with large property variations on short radial distances.

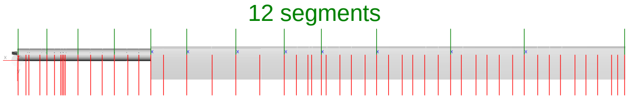

Figure 4: Rotor blade discretization into segments and elements

The propeller moment, which leads to centrifugal stiffening of torsion modes, is not inherently captured by the 1D-beam formulation of SIMBEAM and thus, is modeled via force elements[13]. The blade element propeller moment $M_{\mathrm{P}}^{\mathrm{elem}}$ depends on rotor speed Ω, the difference of flapwise and lagwise blade element inertia $J_{\mathrm{flap}}^{\mathrm{elem}} - J_{\mathrm{lag}}^{\mathrm{elem}}$ and the blade element pitch θ^{elem} with respect to the rotor plane.

$$(7) \quad M_{\mathrm{P}}^{\mathrm{elem}} = \Omega^2 \cdot \left(J_{\mathrm{flap}}^{\mathrm{elem}} - J_{\mathrm{lag}}^{\mathrm{elem}}\right) \cdot \sin\theta^{\mathrm{elem}} \cdot \cos\theta^{\mathrm{elem}}$$

For verification, the rotating blade is linearized at different rotor speeds Ω (but for each linearization, the constraint $\Omega = const.$ holds). The obtained Eigenfrequencies are compared to those computed by the well-validated S4-FEM. The correlation is shown in Figure 5 for the first five flap modes, three lead-lag modes and two torsion modes. The rise in first torsion Eigenfrequency with increasing rotor speed Ω shows the accurate implementation of the propeller moment in SIMPACK. The second torsion Eigenfrequency in SIMPACK slightly diverges from the S4-FEM predictions but is still acceptable. All other modes show a very good correlation for the whole range of Ω, i. e. the corresponding graphs in Figure 5 are mostly congruent in the applied resolution.

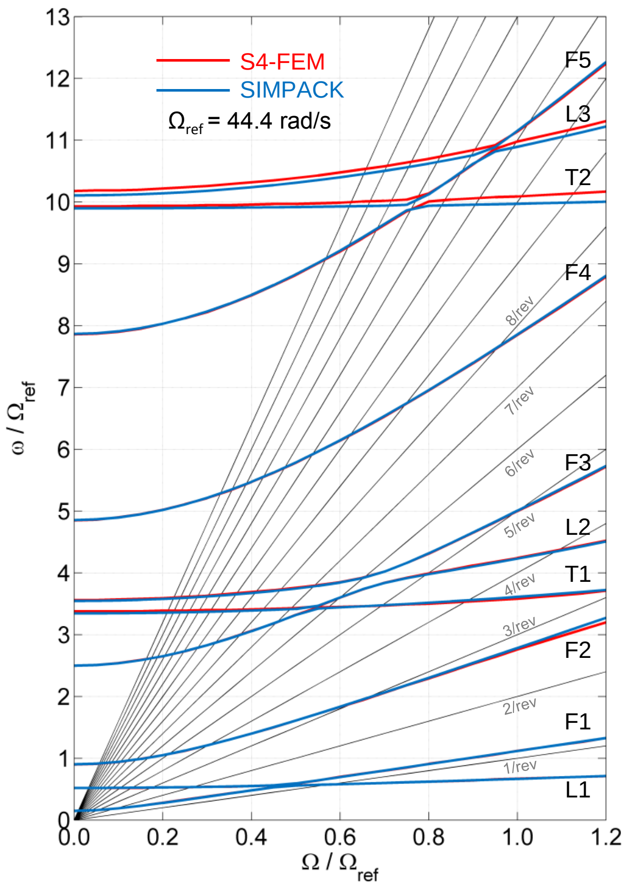

Figure 5: Correlation of the Bo105 blade Eigenfrequencies between SIMPACK and S4-FEM. No offset between mass axis and elastic axis

4. ROTOR-DRIVETRAIN SYSTEM ANALYSIS

The Eigenfrequencies in Figure 5 are based on the hub constraint $\Omega = const$. This constraint is equivalent to an infinite condensed drivetrain inertia J_{DT}, attached to a freely rotating hub via an infinite condensed drivetrain stiffness k_{DT} as depicted in Figure 6. When only a single blade is considered (as in Figure 6), J_{DT} and k_{DT} represent the parameters of an actual drivetrain divided by the blade number.

4.1. Effect of Finite Drivetrain Inertia

The blade model illustrated in Figure 6 is linearized sequentially at varying rotor speed Ω and varying inertia J_{DT}. The stiffness is set to the extremely high (quasi-infinite) value of $k_{\mathrm{DT}} = 10^9\,\mathrm{Nm/rad}$, which lies several orders of magnitude above the realistic stiffness. Only the lead-lag modes of the rotor blade are considered. Flap and torsion modes are suppressed through extremely high related blade stiffnesses.

The resulting Eigenfrequencies of the first lead-

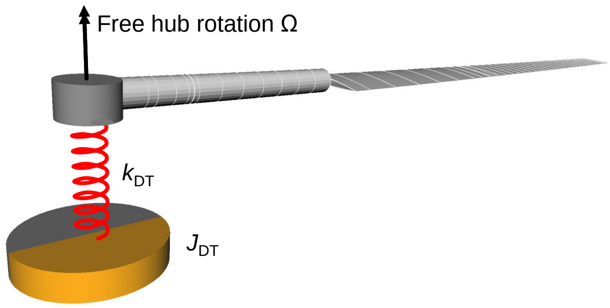

Figure 6: Freely rotating blade connected to inertia J_{DT} via torsional stiffness k_{DT}

lag mode L1 are shown in Figure 7. The baseline case (constrained hub with $\Omega = const.$) is $J_{DT}/J_{DT}^{accu} = \infty$. $J_{DT}^{accu} = 51.25\,\mathrm{kgm}^2$ is the accumulated inertia of all Bo105 drivetrain components below the rotor hub, divided by the blade number. Thus, $J_{DT}/J_{DT}^{accu} = 1$ represents a realistic drivetrain inertia.

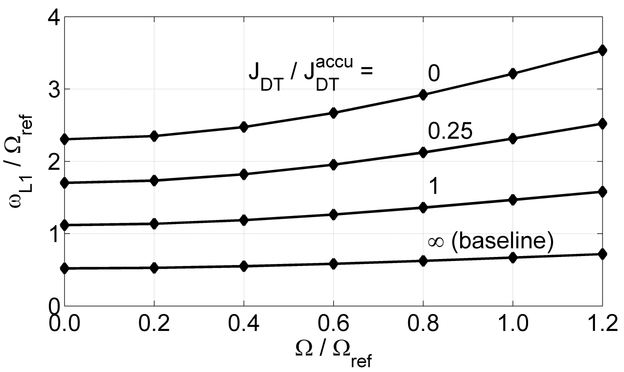

Figure 7: Influence of rotor speed Ω and coupled inertia J_{DT} on the blade's first lead-lag Eigenfrequency ω_{L1}. $k_{DT} = \infty$

As expected from consideration of a linear mass-spring-oscillator ($\omega^2 = k_{DT}/J_{DT}$), decreasing inertia causes increasing Eigenfrequency. This effect is abbreviated as "$J_{DT} \downarrow \Rightarrow \omega \uparrow$" in the following. At nominal rotor speed $\Omega = \Omega_{ref}$, the reduction from $J_{DT} = \infty$ (baseline case) to $J_{DT} = J_{DT}^{accu}$ lifts the first lead-lag Eigenfrequency from $\omega/\Omega_{ref} = 0.67$ to $\omega/\Omega_{ref} = 1.47$ – a remarkable increase by factor 2.19. For $J_{DT} \to 0$, the Eigenfrequency converges to a value of $\omega/\Omega_{ref} = 3.21$ (4.79 times higher than baseline case), which corresponds to a freely rotating blade root. The described dependency and the relative changes in Eigenfrequency are similar for all other rotor speeds Ω.

Figure 8 shows the dependency of the first to fourth lead-lag mode on drivetrain inertia J_{DT} at nominal rotor speed $\Omega = \Omega_{ref}$. The logarithmic scale appropriately resolves all potential orders of magnitude for J_{DT}. Note that the scale of J_{DT} is reversed so that the baseline case $J_{DT} = \infty$ is represented by the left side of the figure. The particular graph labeling ("baseline" left, "free-free" right) will be explained by Figure 9. In general, all Eigenfrequencies rise with decreasing inertia. However, the change from $J_{DT} = \infty$ to $J_{DT} = J_{DT}^{accu}$ only affects the first lead-lag mode considerably. The higher modes would only be changed through a drivetrain inertia J_{DT} which is at least one order of magnitude lower. Consequently, the application of a realistic inertia J_{DT}^{accu} (instead of infinite inertia in the baseline case) primarily affects the first lead-lag Eigenfrequency, while the influence on the higher modes is much smaller.

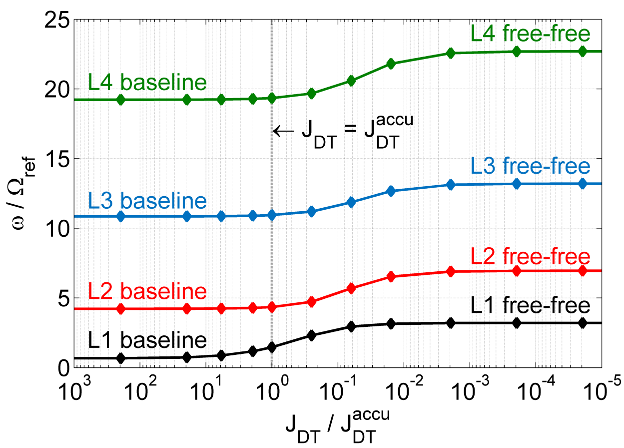

Figure 8: Influence of coupled inertia J_{DT} on blade lead-lag Eigenfrequencies. $\Omega = \Omega_{ref}$, $k_{DT} = \infty$

Along with the lead-lag Eigenfrequencies, the corresponding mode shapes are changed. As an example, Figure 9 illustrates the evolution of the second lead-lag mode shape at nominal rotor speed $\Omega = \Omega_{ref}$ when the drivetrain inertia is reduced from $J_{DT} = \infty$ (baseline case) to $J_{DT} = 0$. Continuously, the shape turns into the second lead-lag shape with "free-free"-boundary condition. For $J_{DT} = J_{DT}^{accu}$, the shape resembles the baseline L2-shape rather than the "free-free" L2-shape. This finding is consistent with the observation from Figure 8, where the L2-Eigenfrequency has barely increased due to the change from $J_{DT} = \infty$ to $J_{DT} = J_{DT}^{accu}$.

4.2. Effect of Finite Drivetrain Stiffness

The influence of rotor speed Ω and varying stiffness k_{DT} on the first lead-lag Eigenfrequency is visualized in Figure 10. Drivetrain inertia is set to the quasi-infinite value of $J_{DT} = 10^9\,\mathrm{kgm}^2$. The baseline case (constrained hub with $\Omega = const.$) is

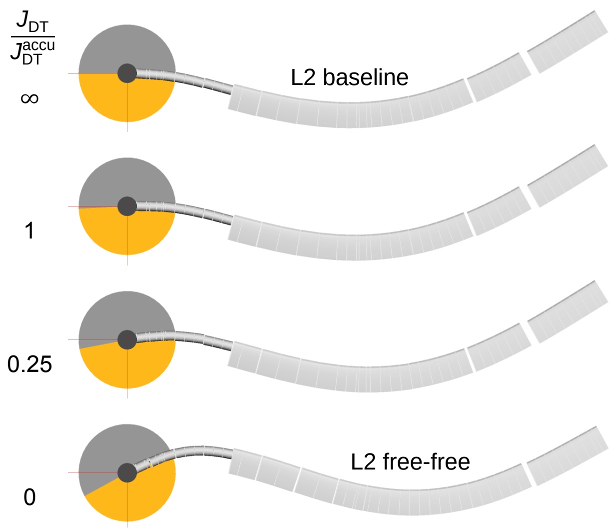

Figure 9: Evolution of L2 mode shape in the course of J_{DT} reduction from ∞ to 0. $\Omega = \Omega_{ref}$, $k_{DT} = \infty$

$k_{DT}/k_{DT}^{accu} = \infty$. The accumulated stiffness $k_{DT}^{accu} = 111.5 \cdot 10^3$ Nm/rad includes all flexible elements in the load path between the rotor hub and the engines' low pressure stages of the Bo105 drivetrain, divided by the blade number.

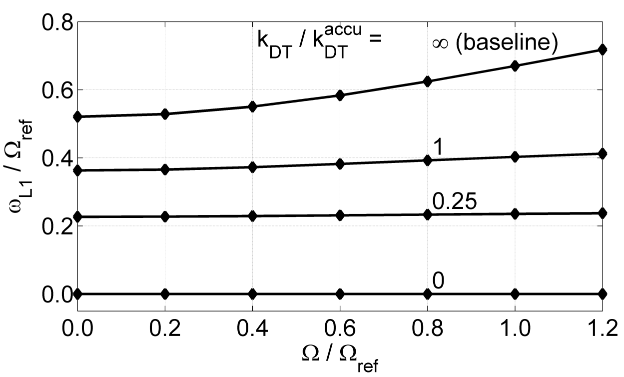

Figure 10: Influence of rotor speed Ω and stiffness k_{DT} on the blade's first lead-lag Eigenfrequency ω_{L1}. $J_{DT} = \infty$

As expected from "$\omega^2 = k_{DT}/J_{DT}$", decreasing stiffness k_{DT} lowers the lead-lag Eigenfrequency ω. This effect is abbreviated as "$k_{DT} \downarrow \Rightarrow \omega \downarrow$" in the following. For $k_{DT} = k_{DT}^{accu}$ (Bo105 drivetrain), the first lead-lag Eigenfrequency is $\omega/\Omega_{ref} = 0.40$, which is smaller by a factor of 0.6 compared to the baseline case ($k_{DT}/k_{DT}^{accu} = \infty$ resulting in $\omega/\Omega_{ref} = 0.67$). For $k_{DT} \rightarrow 0$, ω converges to zero. Then, deformation primarily occurs in the drivetrain rather than in the rotor blade. The described dependency is similar for all other rotor speeds Ω.

Figure 11 shows the Eigenfrequencies of the first to fourth lead-lag mode at $\Omega = \Omega_{ref}$ as a function of drivetrain stiffness k_{DT}. The scale for k_{DT} is logarithmic and reversed, i. e. the baseline case $k_{DT} = \infty$ is represented by the left side of the figure. Decreasing k_{DT} lowers all lead-lag Eigenfrequencies. Compared to the effect of drivetrain inertia, an important difference is observed: The change from $k_{DT} = \infty$ to the realistic stiffness $k_{DT} = k_{DT}^{accu}$ considerably affects all lead-lag modes, since the Eigenfrequency drops of all modes already occur at stiffness values that are about one order of magnitude higher than k_{DT}^{accu}.

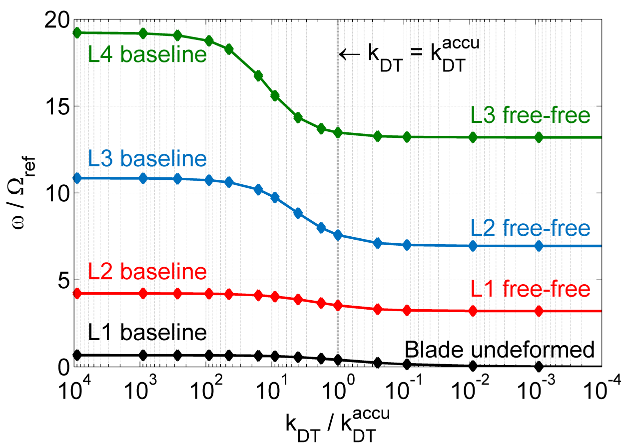

Figure 11: Influence of stiffness k_{DT} on blade lead-lag Eigenfrequencies. $\Omega = \Omega_{ref}$, $J_{DT} = \infty$

It should be noted that due to decreasing drivetrain stiffness k_{DT}, the lead-lag modes change from Li baseline to $L(i-1)$ "free-free". For a better understanding of this correlation, Figure 12 illustrates the evolution of the L2 mode shape due to reduction in k_{DT}. When k_{DT} is reduced from its baseline value $k_{DT} = \infty$, the blade root distortion increases, and the point of inflection moves to the rotor center. From $k_{DT}/k_{DT}^{accu} = 4$ to $k_{DT}/k_{DT}^{accu} = 1$, the point of inflection vanishes. Consequently, for realistic stiffness $k_{DT} = k_{DT}^{accu}$, the modified L2-shape resembles the "free-free" L1-shape rather than the baseline L2-shape. In the following, the modified Li-modes will be called "RD_{Li}" (Rotor-Drivetrain). The mode number i will refer to the baseline mode shape. This means, for example, that although the modified L2-mode rather looks like a L1-mode (but with free-free boundary condition), it will be called "RD_{L2}".

4.3. Rotor-Drivetrain Modes of the Bo105

After the pre-considerations of chapters 4.1 and 4.2, the complete drivetrain model is coupled to the four-bladed Bo105 main rotor. Linearization at

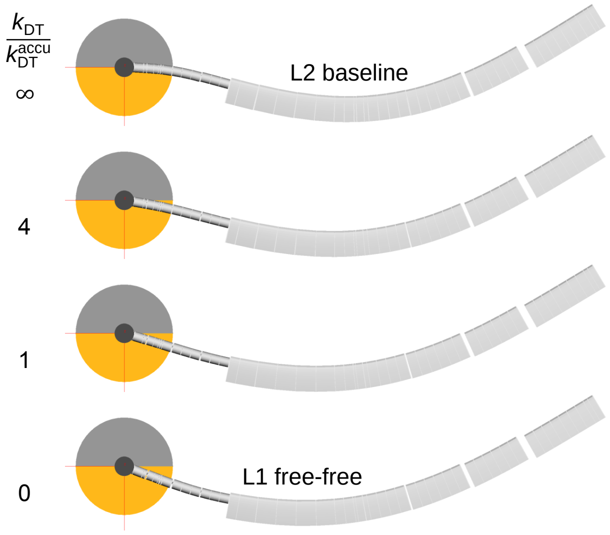

Figure 12: Evolution of L2 mode shape in the course of k_{DT} reduction from ∞ to 0. $\Omega = \Omega_{ref}$, $J_{DT} = \infty$

Table 3: Comparison of Eigenfrequencies at nominal rotor speed. Baseline vs. coupled rotor-drivetrain

Baseline $\Omega = const.$ Mode	ω/Ω_{ref}	Main contri-butions	**R**otor-**D**rivetrain Mode	ω/Ω_{ref}
–	–		**RD$_{TR}$***	**0.60**
L1 (4x)	0.66		L1 (3x)	0.66
–	–		**RD$_{L1}$**	**1.02**
F1 (4x)	1.12		F1 (4x)	1.12
F2 (4x)	2.74		F2 (4x)	2.74
–	–		**RD$_{L2}$**	**3.56**
T1 (4x)	3.67		T1 (3x)	3.67
–	–		**RD$_{T1}$**	**3.68**
L2 (4x)	4.23		L2 (3x)	4.23
F3 (4x)	4.99		F3 (4x)	4.99
F4 (4x)	7.82		F4 (4x)	7.82
–	–		**RD$_{L3}$**	**8.40**
–	–		**RD$_{E}$***	**8.62**

*$\mathbf{RD}$-subscripts: TR = tail rotor, E = engines

nominal rotor speed $\Omega = \Omega_{ref}$ (but with perturbations of Ω allowed) yields the Eigenfrequencies shown on the right side of Table 3, whereas the baseline frequencies ($\Omega = const.$) are listed to the left.

It has been proved by experiment[15] and analytically[14], that only collective rotor modes are affected by the drivetrain. At the remaining modes (four-bladed rotor: longitudinal, lateral, differential), blade root bending moments at the hub cancel each other out. Hence, as an example, the first lead-lag mode of the coupled rotor-drivetrain-system occurs three times unchanged (L1 at $\omega/\Omega_{ref} = 0.66$), while the collective mode transforms to a rotor-drivetrain mode (RD$_{L1}$) at a higher Eigenfrequency of $\omega/\Omega_{ref} = 1.02$. This correlation is indicated by the arrows in Table 3.

Discussion of RD$_{L1}$ mode

The Eigenfrequency of the RD$_{L1}$ mode[¶] $\omega/\Omega_{ref} = 1.02$ is 1.54 times higher than that of the uncoupled L1 mode ($\omega/\Omega_{ref} = 0.66$). As explained before, this rise in Eigenfrequency is caused by the effect of drivetrain inertia. However, the factor of 1.54 lies significantly below 2.19, as obtained with infinite drivetrain stiffness (cf. discussion of Figure 7). In conclusion, drivetrain flexibility ($k_{DT} \downarrow \Rightarrow \omega \downarrow$) must not be neglected for the RD$_{L1}$ mode, even though inertia influence ($J_{DT} \downarrow \Rightarrow \omega \uparrow$) dominates.

The Eigenvector of the RD$_{L1}$ mode is illustrated in Figure 13. The top view of the main rotor clearly shows the similarity to the first collective lead-lag mode (L1) of the baseline rotor. In contrast, nodes are present at a non-zero radial station of the blade axis. Below the main rotor, the abstracted representation of the drivetrain is shown. The grey arrows represent the torsional oscillation amplitudes of the inertia elements, corresponding to the main rotor deformation illustrated above. For comparability, the amplitudes are scaled to main rotor speed by the corresponding transmission ratio. The entire drivetrain contributes with large amplitudes. Major deformations are observed in the mast and in the tail rotor shaft. One additional node is present in the tail rotor shaft, i. e. the tail rotor oscillates in reverse phase. Consequently, the tail rotor inertia does not contribute to increase an effective, condensed drivetrain inertia J_{DT} as used in chapter 4.1. This issue has to be respected when parameterizing a condensed drivetrain model.

Discussion of RD$_{L2}$ mode

The Eigenfrequency of the RD$_{L2}$ mode $\omega/\Omega_{ref} = 3.56$ is lower by the factor of 0.84 compared to the uncoupled L2 mode ($\omega/\Omega_{ref} = 4.23$). Thus, in contrast to RD$_{L1}$, the effect of drivetrain stiffness ($k_{DT} \downarrow \Rightarrow \omega \downarrow$, chapter 4.2) dominates.

Figure 14 depicts the RD$_{L2}$ mode shape. Compared to RD$_{L1}$, the nodes in the rotor plane are located further out. A point of inflection, featured by the uncoupled L2 mode, is not visible in the rotor plane. This observation has already been adressed

¶In literature, the RD$_{L1}$ mode is occasionally referred to as the "first torsional mode" of the rotor-drivetrain system.

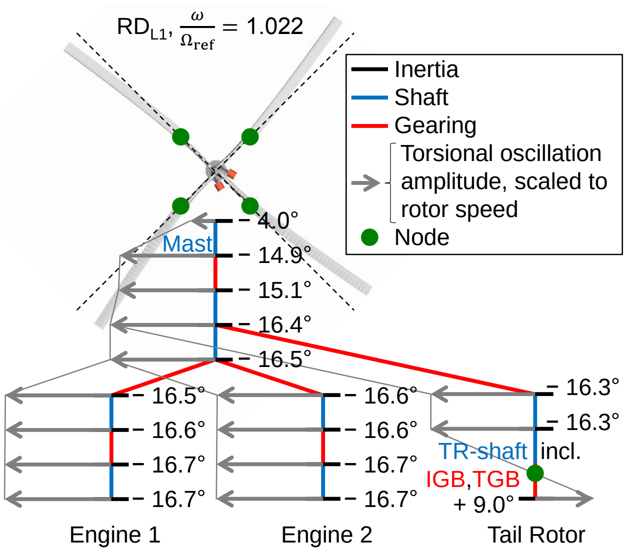

Figure 13: Collective L1 mode transforms to RD$_{L1}$ mode due to rotor-drivetrain-coupling

in the description of Figure 12: The blade mode shape of RD$_{L2}$ resembles the "free-free" L1-mode rather than the uncoupled, baseline L2-mode. Compared to RD$_{L1}$, RD$_{L2}$ features a further node in the main gearbox. Considerable deformation is observed in the rotor mast. Its flexibility decouples the rest of the drivetrain, that shows very weak contribution. As can be seen at the blade tips, the RD$_{L2}$ mode includes slight torsional blade deformation. This is indicated by the dotted arrow in Table 3.

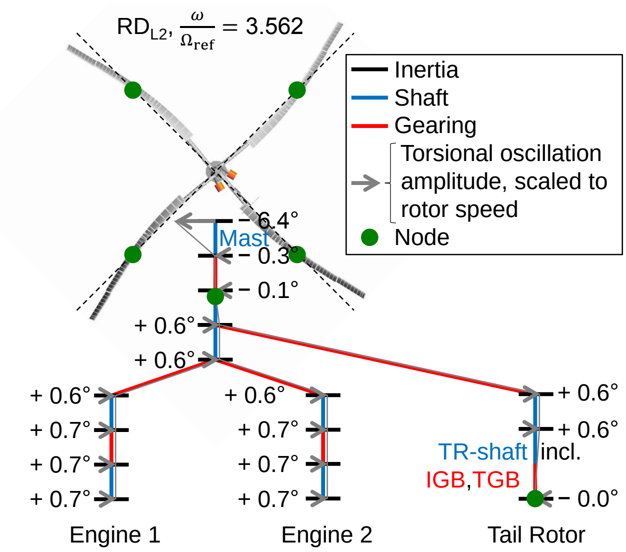

Figure 14: RD$_{L2}$ mode with primary contribution of collective L2 and slight inclusion of collective T1

Discussion of RD$_{L3}$ mode

The Eigenfrequency reduction of the third collective lead-lag mode L3 due to drivetrain influence is even stronger than that of L2. The L3 mode at $\omega/\Omega_{\mathrm{ref}} = 10.89$ transforms to RD$_{L3}$ at $\omega/\Omega_{\mathrm{ref}} = 8.40$ (factor 0.77).

The corresponding mode shape is visualized in Figure 15. Two nodes and one point of inflection per blade are present in the rotor plane. The mast deformation is exceptionally strong compared to the rest of the drivetrain. The decoupling effect on all other drivetrain components is even stronger than in the RD$_{L2}$ mode.

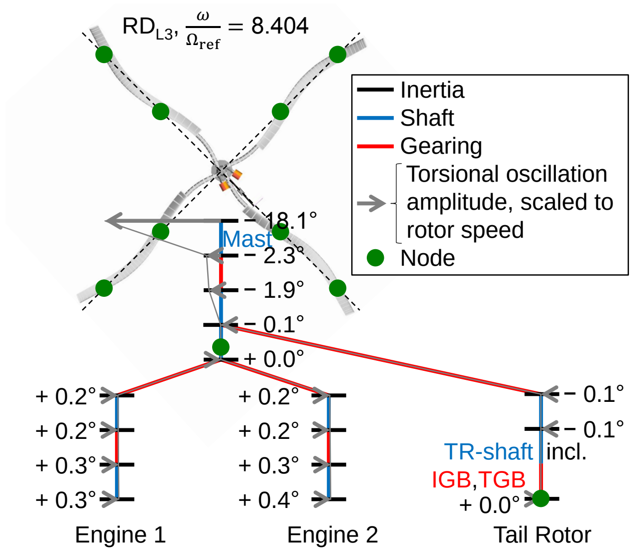

Figure 15: Collective L3 mode transforms to RD$_{L3}$ mode due to rotor-drivetrain-coupling

Further RD modes

The remaining rotor-drivetrain modes are only discussed briefly. The first collective torsional mode is marginally affected by the drivetrain. The RD$_{T1}$ Eigenfrequency is $0.3\,\%$ higher than that of T1. Figure A.1 in the appendix shows the related mode shape. Drivetrain influence on collective flap Eigenfrequencies F1 to F4 causes changes of $0.2\,\%$ maximum and is therefore negligible. The modes RD$_{TR}$ (tail rotor vs. main rotor) and RD$_{E}$ (engines against each other) do not feature considerable main rotor deformation. The corresponding mode shapes are shown in the appendix, figures A.2 and A.3.

4.4. Sensitivity Analysis

The rotor-drivetrain-system of the Bo105 has been modeled to the best of knowledge. However, modeling inacurracies may be inherent in the system. Since experimental validation data of rotor-drivetrain modes is not available, the sensitivity of Eigenfrequencies to potentially inaccurate parameters is investigated in the following.

Rotor parameters

The applied blade mass and stiffness distributions have been validated with S4 in the past, and therefore are considered correct. In contrast, the effect of three particular parameters on rotor-drivetrain modes is not well known.

First, the offset between blade mass axis and elastic axis is investigated in the range $0 \ldots 48\,\mathrm{mm}$ ($\widehat{=} 0 \ldots 18\,\%$ chord; mass axis behind elastic axis). The offset of the “reference configuration” applied in chapter 4.3 is 24 mm. As shown in Figure 16 (left), the influence on $\mathrm{RD_{TR}}$, $\mathrm{RD_{L1}}$ and $\mathrm{RD_{L2}}$ is insignificant. Only the $\mathrm{RD_{T1}}$-Eigenfrequency is affected by the flap-torsion coupling due to mass offset, along with the F2 and T1 modes. This is an effect on the uncoupled modes, not on rotor-drivetrain modes.

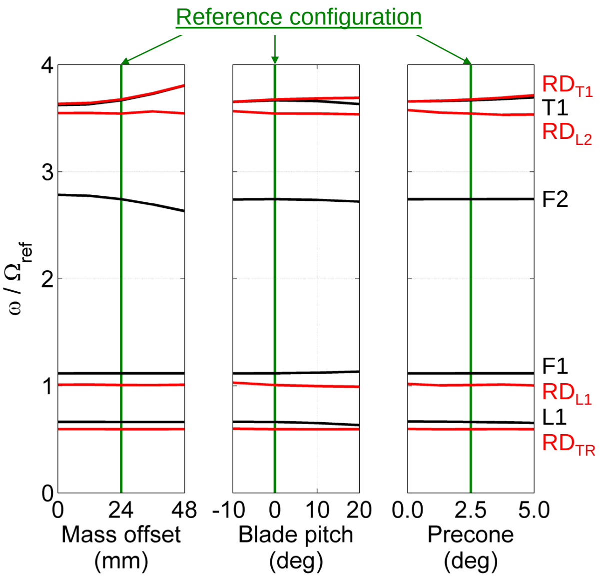

Figure 16: Influence of rotor parameters on the Eigenfrequencies of the rotor-drivetrain system. The reference configuration, used in chapter 4.3, is marked in green. $\Omega = \Omega_{\mathrm{ref}}$.

Second, the blade pitch angle is varied to capture the effect of elastic coupling between flap and lag motion and to assess its influence on the rotor-drivetrain modes (Figure 16, middle). Between $-10°$ and $20°$ (reference $= 0°$), no significant change of rotor-drivetrain Eigenfrequencies is observed. Obviously, the change in L1 and L2 Eigenfrequency due to elastic coupling is so small that the rotor-drivetrain modes $\mathrm{RD_{L1}}$ and $\mathrm{RD_{L2}}$ are not affected remarkably.

Third, the blade precone angle is changed in the range $0 \ldots 5°$ (reference $= 2.5°$) to assess the influence of the related torsion-lag coupling on the rotor-drivetrain modes (Figure 16, right). At $0°$ precone, the Eigenfrequencies of T1 and $\mathrm{RD_{T1}}$ are identical, meaning that drivetrain and collective torsion are decoupled. $\mathrm{RD_{T1}}$ is not an acutal rotor-drivetrain mode in this case. Only with non-zero precone angle, the collective torsional mode is lifted in Eigenfrequency by the drivetrain and turns into a “real” $\mathrm{RD_{T1}}$ mode. This can be explained by the coupling to $\mathrm{RD_{L2}}$, which is simultaneously decreased in Eigenfrequency.

All in all, the evaluated rotor parameters have a noticeable but weak influence on the rotor-drivetrain modes. Though, a non-zero precone angle enables torsion-lag interaction which in turn couples torsion and drivetrain in the $\mathrm{RD_{T1}}$ mode.

Drivetrain parameters

The drivetrain model from chapter 2.3 is parameterized by 16 inertia values and 11 stiffness values. Hence, the condensed model from Figure 6 is chosen instead to keep a clear overview of parameter variations. Prior to variations, the reference parameter set is optimized to accurately represent the Bo105 drivetrain. In contrast to the accumulated parameters $J_{\mathrm{DT}}^{\mathrm{accu}}$ and $k_{\mathrm{DT}}^{\mathrm{accu}}$ from chapters 4.1 and 4.2, the parameters $J_{\mathrm{DT}}^{\mathrm{ad}}$ and $k_{\mathrm{DT}}^{\mathrm{ad}}$ are adapted iteratively. The two corresponding iteration objectives are the Eigenfrequencies $\mathrm{RD_{L1}}$ and $\mathrm{RD_{L2}}$ from chapter 4.3. A unique solution is found. It is remarkable that the adapted parameters differ significantly from the accumulated parameters, as listed in Table 4[||].

Table 4: Parameters of the condensed drivetrain model in Figure 6, accumulated vs. adapted.

method	J_{DT} ($\mathrm{kgm^2}$)	k_{DT} ($10^3\,\mathrm{Nm/rad}$)
accumulated (chapters 4.1 and 4.2)	205.00	446.00
adapted (chapter 4.4)	164.08	462.23

[||] The parameters of Table 4 apply to a four-bladed rotor, whereas the values in chapters 4.1 and 4.2 refer to a single blade (consider factor 4).

J_{DT}^{ad} is 20 % smaller than J_{DT}^{accu}. The main reason is the tail rotor, which makes up 13 % of J_{DT}^{accu}. As mentionend in the discussion of Figure 13, it oscillates in reverse phase with respect to the rest of the drivetrain and therefore does not add to the effective drivetrain inertia. Consequently, J_{DT}^{ad} is smaller than J_{DT}^{accu}. A further reason for J_{DT}^{ad} being lower than J_{DT}^{accu} is the distribution of inertia elements throughout the drivetrain. The inertias of the main gearbox elements are not located at the end, but within the flexible connection between rotor hub and engines. Consequently, the effective inertia at the end is smaller. Analogously, due to distribution of stiffness elements throughout the drivetrain, k_{DT}^{ad} is 4 % larger than k_{DT}^{accu}.

Around the reference configuration of the condensed model $\left[J_{DT}^{ad}, k_{DT}^{ad}\right]$, drivetrain inertia is varied at constant stiffness and vice versa. Large ranges of $k_{DT} = 70...160\,\%\, k_{DT}^{ad}$ and $J_{DT} = 60...120\,\%\, J_{DT}^{ad}$ are investigated. The resulting Eigenfrequencies of the rotor-drivetrain system are depicted in Figure 17. Due to the condensed drivetrain model, the RD_{TR} mode has vanished.

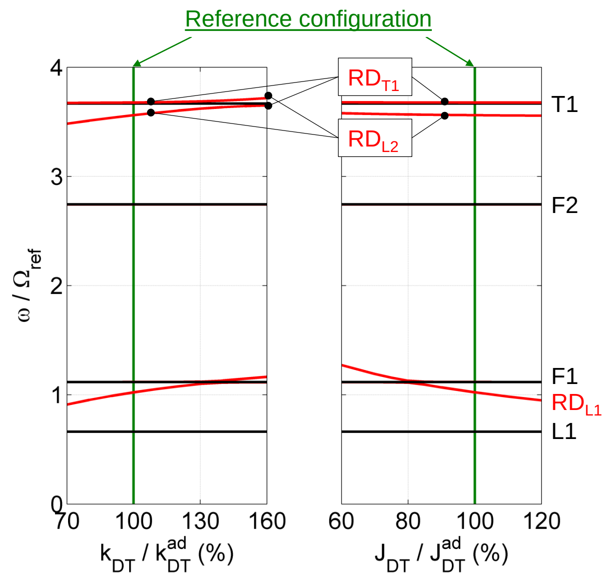

Figure 17: Influence of drivetrain parameters on the Eigenfrequencies of the rotor-drivetrain system. The reference configuration $\left[J_{DT}^{ad}, k_{DT}^{ad}\right]$ is marked in green. $\Omega = \Omega_{ref}$.

Conform to the finding of chapter 4.2, stiffness variation affects both RD_{L1} and RD_{L2}. Increasing drivetrain stiffness k_{DT} lifts the corresponding Eigenfrequencies. At $k_{DT} \approx 140\,\%\, k_{DT}^{ad}$, the Eigenfrequency of RD_{L1} hits that of the first flap mode F1. The collective flap mode couples with the RD_{L1} mode, resulting in two modes. Each of them features flap, lag and drivetrain contributions. In the interval $k_{DT} = 130...160\,\%\, k_{DT}^{ad}$, strong coupling between RD_{L2} and RD_{T1} is observed. There, both rotor-drivetrain modes contain lag, torsion and drivetrain motion.

As found in chapter 4.1, lower drivetrain inertia causes a lift of the RD_{L1}-Eigenfrequency, whereas the higher rotor-drivetrain modes are not affected. For $J_{DT} \approx 80\,\%\, J_{DT}^{ad}$, RD_{L1} couples with the first collective flap mode as described previously.

To conclude the observations from drivetrain parameter variations, rotor-drivetrain modes are significantly affected. For lower stiffness and/or higher inertia than determined for the Bo105 drivetrain, Eigenfrequencies change but the modes remain the same in principle. Higher stiffness and/or lower inertia may lead to a coupling between RD_{L1} and the collective flap mode. Additionally, for higher stiffness than calculated, the coupling between RD_{L2} and RD_{T1} gets stronger.

5. CONCLUSION AND OUTLOOK

Rotor and drivetrain dynamics are coupled via the rotor hub's rotational degree of freedom. The drivetrain influence on the lead-lag modes of hingeless helicopter rotors can be summarized as follows.

Effects of drivetrain inertia and stiffness

Starting from a constrained rotor hub, which is represented by infinite drivetrain inertia, any inertia reduction causes a rise in the Eigenfrequencies of all collective lead-lag modes. However, when applying a realistic drivetrain inertia, only the first collective lead-lag mode is affected considerably. A strong effect on higher collective lead-lag modes would require a drivetrain inertia which is at least one order of magnitude lower compared to the investigated Bo105 configuration.

The decrease of drivetrain stiffness from infinity (baseline case) to realistic values leads to a reduction in the Eigenfrequencies of all collective lead-lag modes. In contrast to the effect of inertia, higher modes are significantly influenced, unless drivetrain stiffness is at least one order of magnitude higher compared to the investigated Bo105 configuration.

Bo105 rotor-drivetrain system

The drivetrain has a considerable influence on the shapes and Eigenfrequencies of the collective lead-lag modes. Based on the determined Bo105 drivetrain parameters, the first collective lead-lag mode turns into the $\mathrm{RD}_{\mathrm{L1}}$ mode with an increase in Eigenfrequency by a factor of 1.54. Thus, the effect of finite drivetrain inertia dominates over the effect of finite drivetrain stiffness.

In contrast, the second collective lead-lag mode is primarily affected by drivetrain stiffness. It transforms into the $\mathrm{RD}_{\mathrm{L2}}$ mode, resulting in an Eigenfrequency decrease by a factor of 0.84 compared to the uncoupled L2 mode.

The collective torsion mode may also interact with the drivetrain, called $\mathrm{RD}_{\mathrm{T1}}$, if a non-zero precone angle is applied. Furthermore, if drivetrain stiffness is higher than calculated in this study, $\mathrm{RD}_{\mathrm{T1}}$ and $\mathrm{RD}_{\mathrm{L2}}$ are strongly coupled.

The collective flap modes and all non-collective modes (four-bladed rotor: longitudinal, lateral, differential) remain unaffected by the drivetrain.

In general, parameter determination of a condensed drivetrain model $[J_{\mathrm{DT}}, k_{\mathrm{DT}}]$ by ordinary accumulation of inertia and stiffness elements is not reliable. The reason is the distribution of inertia and stiffness elements throughout the drivetrain. However, if the parameters of the condensed model are being optimized such that the Eigenfrequencies $\mathrm{RD}_{\mathrm{L1}}$ and $\mathrm{RD}_{\mathrm{L2}}$ match those of the full model, a valuable simplified model for rotor-drivetrain interaction studies is obtained.

Future Work

The presented structural analysis provides the basis for thorough understanding of dynamic rotor-drivetrain interaction. The overall objective is the assessment of drivetrain influence on rotor blade lead-lag loads of hingeless helicopters. The next step towards this goal is the inclusion of excitations and investigation of rotor-drivetrain response in a time domain simulation. Excitations are primarily the airloads acting at the main rotor, but also engine dynamics acting at the other end of the rotor-drivetrain system.

The primary aerodynamic excitation of rotor-drivetrain modes is assumed to act at blade passage frequency, $4\,\Omega$ in case of the Bo105. Since the detected Eigenfrequencies of the $\mathrm{RD}_{\mathrm{L2}}$ and $\mathrm{RD}_{\mathrm{T1}}$ modes lie close to this frequency, a notable drivetrain influence on the lead-lag loads is expected.

6. ACKNOWLEDGEMENTS

The authors like to thank Oliver Dieterich and Heinrich Schweitzer from Airbus Helicopters for insightful discussions on rotor-drivetrain interaction and for the supply of tail rotor related data. Furthermore, the authors express their gratitude to Maximilian Mindt from DLR, who contributed considerably to the successful rotor modeling in SIMPACK by his experience and advice.

A. APPENDIX

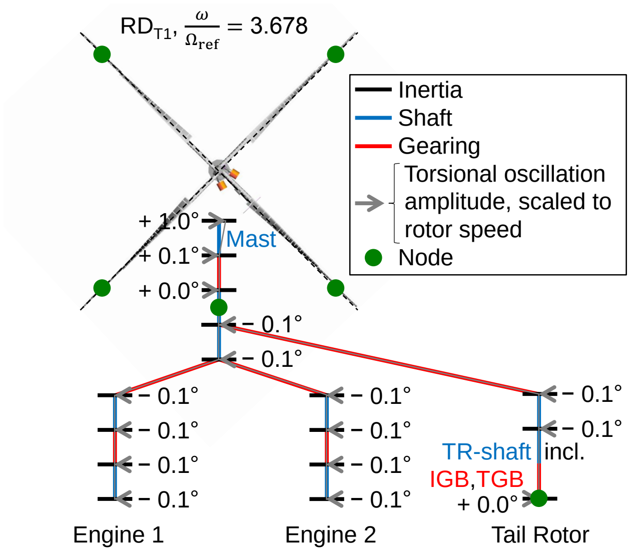

Figure A.1: $\mathrm{RD}_{\mathrm{T1}}$ mode with primary contribution of collective T1 and slight inclusion of collective L2, which is the cause of drivetrain coupling

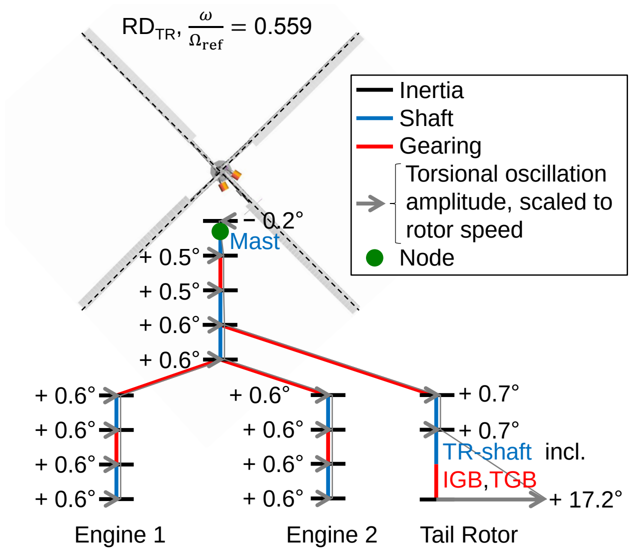

Figure A.2: RD$_{TR}$ mode: "Tail rotor vs. main rotor". No considerable deformation in the main rotor

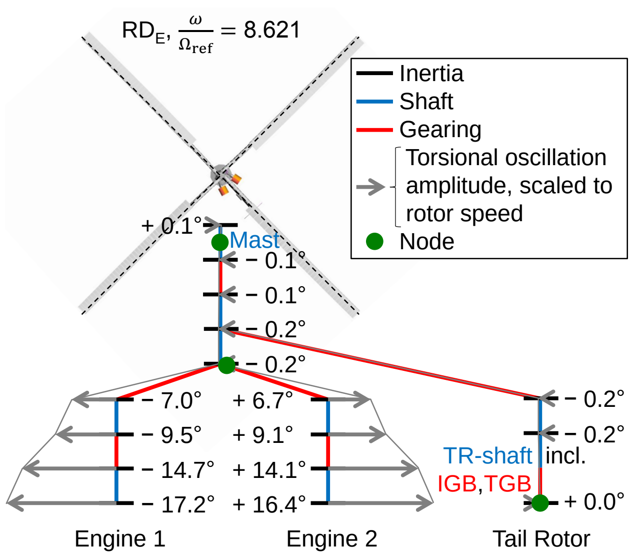

Figure A.3: RD$_E$ mode: "Engines against each other". No considerable deformation in the rest of the rotor-drivetrain system

REFERENCES

[1] Dieterich, O., Langer, H.-J., Schneider, O., Imbert, G., Hounjet, M. H. L., Riziotis, V., Cafarelli, I., Calvo Alonso, R., Clerc, C., and Pengel, K., "HeliNOVI: Current Vibration Research Activities," *31st European Rotorcraft Forum*, Florence, Italy, Sept. 2005.

[2] Yeo, H. and Potsdam, M., "Rotor Structural Loads Analysis Using Coupled Computational Fluid Dynamics/Computational Structural Dynamics," *Journal of Aircraft*, Vol. 53, No. 1, 2016, pp. 87–105.

[3] Makinen, S. M., Wake, B. E., and Opoku, D., "Quantitative Evaluation of Rotor Load Prediction Results Correlated to Flight Test Data," *AHS 66th Annual Forum*, Virginia Beach, Virginia, May 2011.

[4] Ahaus, L., Wasikowski, M., Morillo, J., and Louis, M., "Loads Correlation of a Bell M429 Rotor Using CFD/CSD Coupling," *AHS 69th Annual Forum*, Phoenix, Arizona, May 2013.

[5] Abhishek, A., Datta, A., and Chopra, I., "Prediction of UH-60A Structural Loads using Multibody Analysis and Swashplate Dynamics," *AHS 62nd Annual Forum*, Phoenix, Arizona, May 2006.

[6] Sidle, S., Sridharan, A., and Chopra, I., "Coupled Vibration Prediction of Rotor-Airframe-Drivetrain-Engine Dynamics," *AHS 74th Annual Forum*, Phoenix, Arizona, May 2018.

[7] Min, B.-Y., Agarwal, S., Wilbur, I., Smith, M. J., Modarres, R., Zhao, J., Wong, J., and Wake, B. E., "Toward Improved UH-60A Blade Structural Loads Correlation," *AHS 74th Annual Forum*, Phoenix, Arizona, May 2018.

[8] Yeo, H., "UH-60A Rotor Structural Loads Analysis with Fixed-System Structural Dynamics Modeling," *AHS 74th Annual Forum*, Phoenix, Arizona, May 2018.

[9] Laschet, A., *Simulation von Antriebssystemen: Modellbildung der Schwingungssysteme und Beispiele aus der Antriebstechnik*, Springer, Berlin, 1988, ISBN: 978-3-540-19464-4.

[10] Dresig, H., *Schwingungen mechanischer Antriebssysteme – Modellbildung, Berechnung, Analyse, Synthese*, Springer, Berlin, Heidelberg, 2001, ISBN: 978-3-662-09833-2.

[11] Holzweißig, F. and Dresig, H., *Lehrbuch der Maschinendynamik*, Springer, Wien, 1979, ISBN: 978-3-7091-3302-6.

[12] Mindt, M. and Surrey, S., "Investigating the Coupling of Helicopter Aerodynamics with SIMPACK for Articulated and Hingeless Rotors," *65. Deutscher Luft- und Raumfahrtkongress*, Braunschweig, Sept. 2016.

[13] Hofmann, J., Krause, L., Mindt, M., Graser, M., and Surrey, S., "Rotor Simulation and Multibody Systems: Coupling of Helicopter Aerodynamics with SIMPACK," *63. Deutscher Luft- und Raumfahrtkongress*, Augsburg, Sept. 2014.

[14] Jaw, L. C. and Bryson, Jr., A. E., "Modeling Rotor Dynamics with Rotor Speed Degree of Freedom for Drive Train Torsional Stability Analysis," *16th European Rotorcraft Forum*, Glasgow, United Kingdom, Sept. 1990.

[15] Carpenter, P. J. and Peitzer, H. E., "Response of a Helicopter Rotor to Oscillatory Pitch and Throttle Movements," NACA TN 1888, 1949.